ACS Catalysis

Research Article

pubs.acs.org/acscatalysis

Synthesis and Stability of Pd@CeO$_2$ Core–Shell Catalyst Films in Solid Oxide Fuel Cell Anodes

Lawrence Adijanto,[†] Anirudh Sampath,[†] Anthony S. Yu,[†] Matteo Cargnello,[‡] Paolo Fornasiero,[§] Raymond J. Gorte,[†] and John M. Vohs[†,*]

[†]Department of Chemical and Biomolecular Engineering, University of Pennsylvania, 311A Towne Building, 220 South 33rd Street, Philadelphia, Pennsylvania 19104, United States

[‡]Department of Chemistry, University of Pennsylvania, 19104, United States Philadelphia, Pennsylvania, United States.

[§]Department of Chemical and Pharmaceutical Sciences, ICCOM-CNR, Consortium INSTM, University of Trieste, via L. Giorgieri 1, 34127 Trieste, Italy

ABSTRACT: Submonolayer films of highly catalytically active Pd@CeO$_2$ nanocomposites, consisting of a Pd nanoparticle core coated with a porous CeO$_2$ shell, were deposited onto porous solid oxide fuel cell (SOFC) anodes that were functionalized with triethoxy(octyl)silane (TEOOS). SEM results show that in contrast to bare Pd particles, Pd@CeO$_2$ particles grafted onto the surface of the ceramic anode remained highly dispersed, even after calcination in air at 1373 K. SOFC with anodes that were modified with very low loadings (0.01 wt %) of the Pd@CeO$_2$ nanocomposites were shown to exhibit good electrochemical performance when operating with either H$_2$ or CH$_4$ fuels at 973 K. This performance was also maintained after annealing the anode in air at 1173 K. These results demonstrate a strategy for using very low loadings of highly active metal catalysts to enhance the activity of ceramic anodes while maintaining long-term stability.

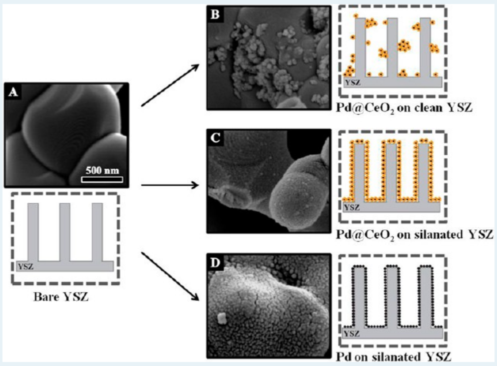

KEYWORDS: *solid oxide fuel cells, catalyst, palladium, cerium dioxide, core–shell nanostructures*

INTRODUCTION

Solid oxide fuel cells (SOFCs) offer scalable, flexible fuel, high-efficiency conversion of the energy stored in chemical fuels into electrical energy. Enhanced performance and stability is needed, however, for these devices to enter the marketplace. This is especially true of the anode side of these cells, which is typically composed of a porous, Ni–YSZ composite (cermet). Although Ni–YSZ cermets are relatively easy to fabricate and Ni has high catalytic activity for H$_2$ oxidation, it is prone to sintering at typical SOFC operating temperatures, has low tolerance to the sulfur impurities that are present in most fuels, promotes coke formation from hydrocarbons, and has low redox stability.[1−9] All of these latter attributes have motivated the search for alternative materials for use as the electrochemically active component in SOFC anodes. A variety of electronically conducting ceramics have been proposed as possible replacements for Ni because these materials would be expected to be less susceptible to sintering and coking and exhibit higher redox stability.[10−30]

Unfortunately, the electrochemical performance of SOFC anodes incorporating conductive ceramics tends to be relatively poor due to the fact that these materials have low catalytic activity for oxidation reactions. Performance comparable to that obtained with Ni–YSZ cermets can be achieved, however, if dopant levels of highly catalytic metals (e.g., Pt or Pd) are added to the surface of the conducting ceramic.[16,20−23,27,29,31−41] For example, anodes containing a functional layer consisting of a porous YSZ backbone coated with an electronically conducting thin film of La$_{0.8}$Sr$_{0.2}$Cr$_{0.5}$Mn$_{0.05}$O$_3$ (LSCM) decorated with catalytic amounts of Pd (1 wt %) have been shown to have anode area specific resistances (ASR) of approximately 0.2 Ω cm^2 when operating on H$_2$ fuel at 973 K,[19] which is comparable to that reported for conventional Ni–YSZ cermet anodes under similar conditions.[42]

Although this approach to anode design clearly holds some promise, the stability of the added catalyst is still an issue, since the metal nanoparticles that are produced using standard wet infiltration techniques tend to sinter at SOFC operating temperatures, resulting in loss in active surface area and a decrease in performance.[12,16,20,43] The loss of activity due to metal catalyst sintering is also an issue in many other applications that require heterogeneous catalysts.[44−54] One approach that has recently been proposed to enhance metal catalyst thermal stability is to encapsulate the metal nanoparticle in a thin, porous metal oxide shell. The oxide coating on these so-called core–shell particles tends to interact strongly with an oxide support, thereby anchoring the metal particle and preventing sintering. Another added benefit of these core–shell particles is that in

Received: May 30, 2013
Revised: July 1, 2013
Published: July 2, 2013

many cases, synergistic interactions between the metal nanoparticle and the oxide shell can enhance catalytic activity.[55−59] For example, $Pd@CeO_2$ nanostructures (i.e., Pd nanoparticle encased in a ceria shell) have been shown to exhibit unusually high catalytic activity for the combustion of methane compared with a conventional Pd supported on CeO_2 catalyst.[55]

Several of us have previously demonstrated the use of $Pd@CeO_2$ nanocomposites to significantly enhance the catalytic oxidation activity of an SOFC anode consisting of a porous YSZ scaffold coated with a thin film of LSCM.[43] In this work, the catalyst was deposited into the anode using infiltration of a $Pd@CeO_2$ dispersion in tetrahydrofuran (THF) solution. Although this produced a high-performance anode that did not undergo significant deactivation due to loss of catalyst surface area upon calcination at 1173 K, a high 10 wt % loading of the $Pd@CeO_2$ (1 wt % Pd and 9 wt % CeO_2) was required to obtain a sufficient concentration of the catalyst particles in the electrochemically active zone near the electrode−electrolyte interface. SEM analysis also indicated that this synthesis method produced large agglomerates of the $Pd@CeO_2$ particles. Given the relatively high cost of Pd, much more efficient use of the catalyst will be required for this method of enhancing anode activity to be practical. This could be achieved by producing a highly dispersed layer of individual $Pd@CeO_2$ particles on the surface of the anode.

To address this issue and obtain high catalyst dispersion, we have recently developed a method to graft individual $Pd@CeO_2$ particles onto an oxide surface.[60] This method relies on initially coating the surface of the oxide support (or anode) with hydrophobic alkyl groups via reaction with triethoxy(octyl)silane (TEOOS) as the surface modifier. The $Pd@CeO_2$ particles are also functionalized with hydrophobic groups to stabilize them in organic solvents such as THF. Upon infiltration, van der Waals interactions between the hydrophobic groups on both the YSZ surface and the $Pd@CeO_2$ particles help them stick to the surface and prevents their agglomeration. The organic groups are then subsequently oxidatively removed by calcination in air. Characterization of the deposition of $Pd@CeO_2$ particles on model planar YSZ single crystal supports has demonstrated that this procedure produces a submonolayer coverage of individual $Pd@CeO_2$ particles.[60]

Although this approach produces a highly dispersed catalyst layer, the functionalization of the oxide surface using an organosilane coupling agent may be problematic for use with SOFC electrodes because Si is known to migrate to the grain boundaries in YSZ (the electrolyte of choice for most SOFCs), and this may detrimentally affect oxygen ion transport, reducing the overall performance.[61−63] Because the amount of SiO_x deposited is quite small (monolayer coverage), we anticipate that its effect on transport properties will not be significant.

In the present study, we have used the deposition method outlined above to control both the loading and dispersion of $Pd@CeO_2$ catalytic nanoparticles in SOFC composite anodes that use a conductive LSCM layer for electron transport. The results of this study demonstrate that a highly dispersed and thermally stable layer of $Pd@CeO_2$ nanostructures can be produced in the porous electrode and that electrodes incorporating less than 0.01 wt % $Pd@CeO_2$ exhibit excellent performance.

■ EXPERIMENTAL METHODS

Solid oxide fuel cells 1 cm in diameter were used in all fuel cell measurements. These cells were fabricated using porous−dense−porous trilayer YSZ wafers that were produced using tape casting methods that have been described in detail previously.[64] For each cell, the dense electrolyte layer was 65 μm thick and 1 cm in diameter. The 60% porous YSZ layers on each side of the dense electrolyte layer were 50 μm thick with a BET surface area 0.3 $m^2\ g^{-1}$.

A 45 wt % portion of Sr-doped lanthanum chromium manganate, $La_{0.8}Sr_{0.2}Cr_{0.5}Mn_{0.5}O_3$ (LSCM), anode was added to one porous layer using multiple cycles of infiltration of an aqueous solution containing dissolved $La(NO_3)_3{\cdot}6H_2O$ (Alfa Aesar, 99.9%), $Sr(NO_3)_2$ (Alfa Aesar, 99%), $Cr(NO_3)_3{\cdot}9H_2O$ (Alfa Aesar, 98.5%), and $Mn(NO_3)_3{\cdot}4H_2O$ (Alfa Aesar, 99.98%) in the appropriate molar ratios, followed by calcination in air at 873 K. After the infiltration steps, the composite anode was calcined to 1473 K for 4 h to form the perovskite structure. A 40 wt % portion of Sr-doped lanthanum ferrite, $La_{0.8}Sr_{0.2}FeO_3$ (LSF), was added to the other porous layer to form a cathode using multiple cycles of infiltration of an aqueous solution containing dissolved $La(NO_3)_3{\cdot}6H_2O$ (Alfa Aesar, 99.9%), $Sr(NO_3)_2$ (Alfa Aesar, 99%), and $Fe(NO_3)_3{\cdot}9H_2O$ (Fisher Scientific) in the appropriate molar ratios, followed by calcination in air at 723 K. Citric acid (Fisher Scientific) was also added as a complexing agent to aid in the formation of a more homogeneous mixture. The composite cathode was then calcined to 1123 K for 4 h to form the perovskite structure. Previous studies have shown that cathodes of this design have an ASR of ∼0.2 $\Omega\ cm^2$ in air at 973 K.[21,65]

The synthesis of the $Pd@CeO_2$ core−shell structures (1:9 Pd/Ce weight ratios) is described in detail in previous publications.[66,67] For most cells, prior to the addition of the catalyst, the surface of the anode (45 wt % of LSCM) was functionalized with long-chain alkyl groups via reaction with triethoxy(octyl)silane (TEOOS, Sigma Aldrich 97.5%). The TEOOS (0.1 mL drop) was added to the porous anode layer by infiltration, followed by calcination to 403 K for 4 h, which was found to be sufficient to induce reaction. The catalyst was then added via infiltration, followed by evaporation of an amount of a 1.5×10^{-3} M $Pd@CeO_2$/THF solution that contained the theoretical number of core−shell particles required to form a monolayer over the TEOOS-treated LSCM surface in the LSCM/YSZ composite anode (this calculation was based on the surface area of the porous YSZ electrode). A similar procedure was also used to deposit uncoated 2 nm Pd particles. The samples were then calcined to 723 and 1123 K in air for 4 h to remove the stabilizing organic ligands. For some cells, an aqueous solution of $(NH_3)_4Pd(NO_3)_2$ (Alfa Aesar, 99.9%) was used to deposit Pd.

The anodes were reduced in humidified H_2 (3% H_2O) at 973 K prior to cell testing with humidified H_2 or dry CH_4. Silver current collectors (paste and wires) were applied to both electrodes for electrical connections, and the cells were mounted onto an alumina tube using a ceramic adhesive (Aremco, Ceramabond 552). All the cell tests were performed with the cathode exposed to ambient air. Electrochemical impedance spectra were measured between 0.1 Hz and 300 kHz with a 1 mA AC perturbation. Both impedance spectra and $V{-}i$ polarization curves were measured using a Gamry Instruments potentiostat.

For scanning electron microscopy (SEM) studies, the sample preparation was similar to that used for the fuel cell anodes as described above, except that the surface of the 60% porous YSZ electrode (without 45 wt % of LSCM) was functionalized with TEOOS prior to addition of the THF solution of $Pd@CeO_2$ and 2 nm uncoated Pd particles. The samples were then calcined to 973 and 1373 K in air for 4 h. The morphological structure of the

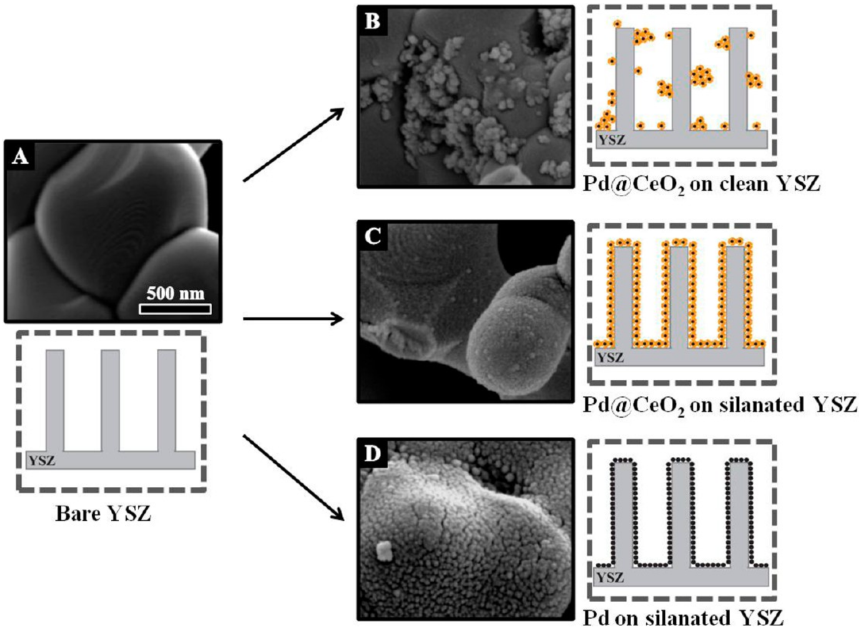

Figure 1. SEM images along with schematic representations of the bare YSZ matrix (panel A), Pd@CeO$_2$ nanoparticles deposited on a clean YSZ porous electrode (panel B) and silanated YSZ porous electrode (panel C). Uncoated Pd nanoparticles (2 nm) deposited on silanated YSZ porous electrode (panel D). All samples calcined at 973 K in air, and the magnification is the same in all of the images.

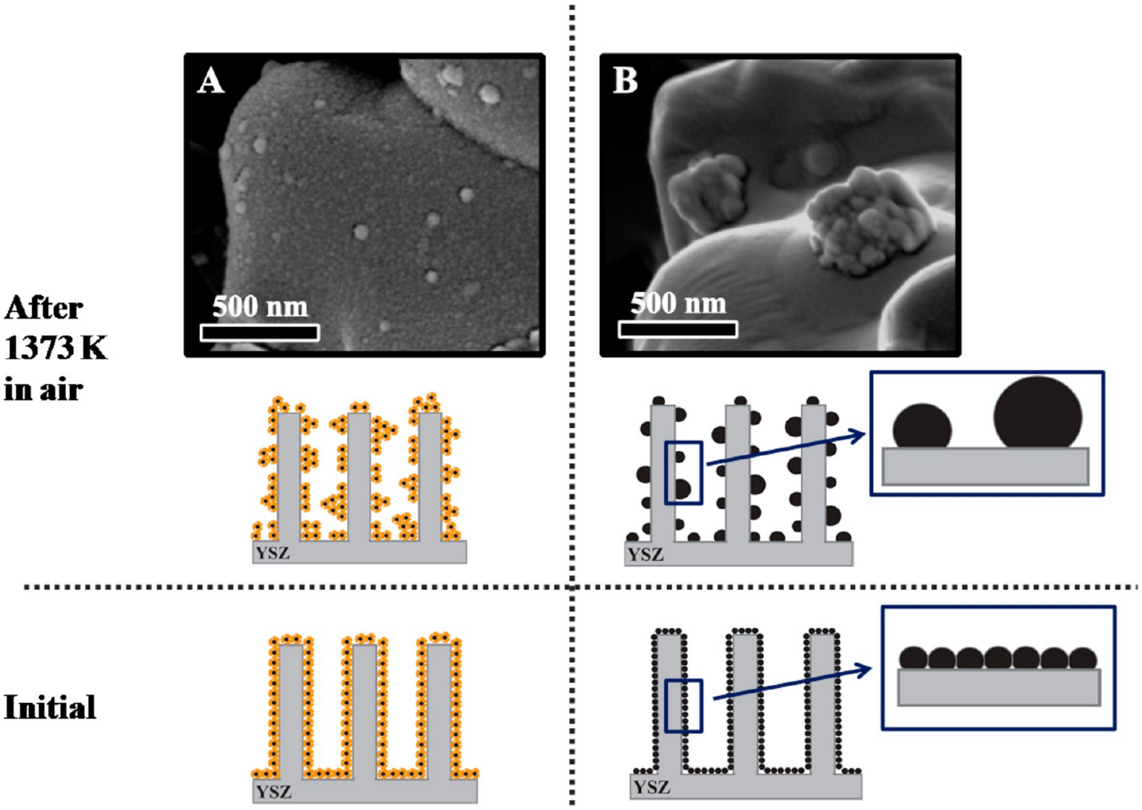

Figure 2. SEM images, with the schematic representation of the agglomeration of Pd@CeO$_2$ (panel A) and 2 nm uncoated Pd (panel B) nanoparticles deposited on silanated YSZ porous electrode after samples calcined at 1373 K in air.

porous composites was determined using an FEI Quanta 600 SEM.

RESULTS AND DISCUSSION

SEM Characterization of Pd@CeO$_2$ on Porous YSZ. As reported previously and described above, nearly monolayer films of highly catalytically active, Pd@CeO$_2$ core−shell nanocomposites can be grafted onto a high surface area metal oxide powders or planar supports which have previously been functionalized with TEOOS.[55,57,60,66,68] SEM was used to assess whether this approach can be used to deposit submonolayer films of Pd@CeO$_2$ onto the surface of a porous SOFC electrode.

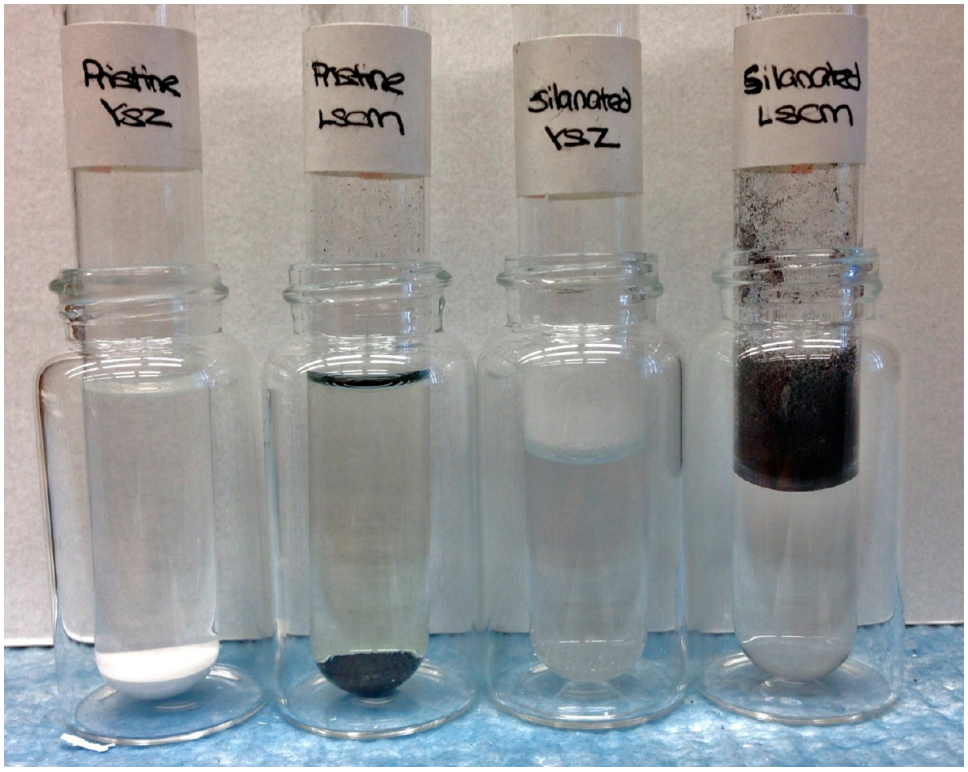

Figure 3. Image of hydropobicity test with YSZ and LSCM before and after treatment with TEOOS. A 0.1 g portion of each powder was then placed in a test tube filled with 5 mL of H_2O.

Because an LSCM thin film is known to undergo microstructural changes upon reduction,[69] in these studies, YSZ was used as the substrate rather than LSCM-coated YSZ to more easily differentiate between the Pd@CeO_2 particles and the support. As described in the experimental section, the surface of a 60% porous YSZ electrode was initially functionalized by reaction with TEOOS and then infiltrated with a THF solution of Pd@CeO_2 that contained the theoretical number of core−shell particles to form a monolayer. The sample was then calcined at 973 K in air for 4 h to remove the organic groups. An SEM image of this sample is displayed in Figure 1. For comparison purposes, SEM images of a TEOOS-treated porous YSZ electrode that was infiltrated with 2 nm Pd particles (i.e., Pd particles without the CeO_2 shell) and a porous YSZ electrode that was not treated with TEOOS prior to deposition of the Pd@CeO_2 particles are also included in the figure.

As we have demonstrated previously,[60] the hydrophobic, alkyl-capped Pd@CeO_2 particles interact only weakly with the hydrophilic, untreated YSZ substrate, which results in the formation of agglomerates of the core−shell particles during the infiltration and subsequent calcination processes. This is demonstrated by the SEM image of the pristine YSZ substrate infiltrated with the Pd@CeO_2/THF solution and then calcined at 973 K in air displayed in Figure 1 (image B). Note that large regions of the substrate are devoid of features while others contain assemblies of the core−shell particles that are not present in the image of the YSZ surface prior to infiltration (image A).

As expected, a significantly different result was obtained when the Pd@CeO_2 nanostructures were deposited onto the TEOOS-treated porous YSZ electrode surface. The TEOOS treatment produces a siloxane layer with attached long alkyl chains, rendering the surface hydrophobic. The hydrophobic Pd@CeO_2 particles can now interact via van der Waals forces with the treated YSZ, which helps disperse them and prevent agglomeration during deposition. As shown in image C in Figure 1, this high dispersion of the Pd@CeO_2 particles is maintained after calcination in air at 973 K to oxidatively remove the organic byproducts. In contrast, agglomeration was obtained for a sample prepared using 2 nm Pd particles that were not coated with CeO_2. These particles were also capped with alkyl groups to stabilize them in the THF solution and would therefore be expected to form a well-dispersed layer upon infiltration into the TEOOS-treated YSZ in a manner similar to that for Pd@CeO_2. Calcination in air at 973 K, however, was sufficient to cause partial agglomeration and sintering of the Pd nanoparticles, as evidenced by the more highly textured surface (larger particles) in the SEM image (image D).

The exceptionally high thermal stability of the Pd@CeO_2 catalyst compared with uncoated Pd particles is more readily apparent in Figure 2, which displays SEM images obtained after heating samples similar to those in Figure 1 to a much higher temperature (1373 K) in air for 4 h. Note that this treatment caused very little change in the structure of the well-dispersed Pd@CeO_2 catalyst layer that had been grafted onto the TEOOS-treated substrate (image A). In contrast, the SEM image for the sample synthesized with the uncoated 2 nm Pd nanoparticles shows extensive sintering of the Pd particles, resulting in the formation of a small number of particles with diameters between 250 and 500 nm. This decrease in dispersion of the Pd and the resulting loss in surface area would be expected to greatly reduce the catalytic activity and performance on an anode. It is noteworthy that these results are consistent with those obtained in our previous AFM study of Pd@CeO_2 and Pd nanoparticles deposited onto a TEOOS-treated planar, single crystal YSZ(100) support.[60]

Althugh these results demonstrate that a high dispersion of $Pd@CeO_2$ particles can be produced on TEOOS-treated YSZ surfaces, an electronically conducting phase, such as LSCM, is required for a working electrode. As noted above, structural characterization of the $Pd@CeO_2$ particles on a LSCM/YSZ composite electrode is problematic because of the complex structure. We have demonstrated, however, that like YSZ, organosiloxane layers can be deposited on LSCM using TEOOS. Evidence for this is presented in Figure 3, which displays photographs of test tubes containing water and a small amount of pristine and TEOOS-treated YSZ or LSCM powders. The surfaces of the pristine powders are terminated with hydroxyl groups, making them hydrophilic, and both the YSZ and LSCM are easily wetted and sink to the bottom of the tube. On the other hand, after treatment with TEOOS, both the YSZ and LSCM powders float on the surface of the water, which is consistent with their being coated with a hydrophobic organosiloxane layer. On the basis of this result, we anticipate that the $Pd@CeO_2$ particles can be grafted onto the LSCM using the same procedure as that demonstrated above for YSZ.

Electrochemical Characterization. *Effect of SiO_2 on the Electrochemical Performance.* It has previously been reported that SiO_x impurities can segregate to the grain boundaries in YSZ and that this can hinder O^{2-} transport.[61−63] Thus, one potential downside of using TEOOS to functionalize the surface of the electrode and facilitate a high dispersion of the $Pd@CeO_2$ particles is that the resulting SiO_x layer may have a deleterious effect on cell performance. To determine the effect, if any, on electrochemical performance due to the SiO_x monolayer produced by reaction of TEOOS on the electrode, two fuel cells with an infiltrated 45 wt % LSCM−YSZ composite anode that had been calcined to 1473 K were fabricated. Both cells had identical LSF−YSZ cathodes and a 65-μm-thick YSZ electrolyte, but only the anode in one of the cells was treated with TEOOS. Both cells were then calcined in air at 723 K, followed by addition of 1 wt % Pd to the anode to enhance the catalytic activity. In this case, to ensure similar catalyst dispersion in both cells, the Pd was added by infiltration of an aqueous solution of $(NH_3)_4Pd(NO_3)_2$. Figure 4 shows the *V*−*i* polarization curves and impedance spectra for the two fuel cells, operating in humidified (3% H_2O) H_2 at 973 K, with the electrochemical performances summarized in Table 1. For comparison purposes, the performance of both cells before the addition of 1 wt % Pd is also included in Table 1.

The *V*−*i* polarization curves (Figure 4A) show that each of the cells had an open-circuit potential near the theoretical Nernst value of 1.1 V. The Nyquist plots of the impedance spectra collected at open circuit (Figure 4B) also show that the ohmic loss for each cell, calculated from the high-frequency intercept with the real axis, was ~0.3 Ω cm^2, which is close to the expected value for the 65-μm-thick YSZ electrolyte. This demonstrates that LSCM provides adequate conductivity for the 50-μm-thick anodes used here. Since LSF−YSZ cathodes identical to those used here have previously been shown to have a specific resistance (ASR) of 0.2 Ω cm^2,[2,21,65] the anode ASR can be obtained by subtracting from the total resistance the ohmic (0.3 Ω cm^2) and cathode contributions. Note that the relatively poor electrochemical performance obtained from both the cells prior to addition of 1 wt % Pd catalyst (Table 1) is due to the low catalytic activity of LSCM. The addition of the Pd catalyst had a dramatic effect on cell performance, with the maximum power density of both cells increasing to 0.39 W cm^{-2} with an anode ASR of only 0.25 Ω cm^2. The fact that a nearly identical performance was obtained for both cells demonstrates that the SiO_x layer that was deposited on the surface of one of the anodes via reaction with TEOOS did not hinder oxygen ion transport from the LSCM to the YSZ electrolyte. Longer-term effects of the SiO_x layer were not studied, and segregation of a portion of the SiO_x to grain boundaries could affect performance, but given the small amount of TEOOS that is used, it seems unlikely that this would be problematic.

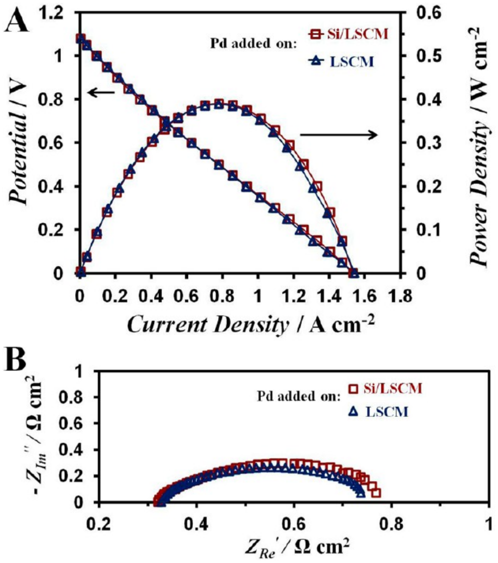

Figure 4. (A) *V*−*i* polarization curves and (B) electrochemical impedance spectra of cells with infiltrated 45 wt % LSCM−YSZ (blue Δ) with and (red ☐) without treatment with TEOOS. Both the cells were then calcined in air at 723 K upon addition of 1 wt % Pd to the TEOOS-treated LSCM anode by infiltration with aqueous solution of $(NH_3)_4Pd(NO_3)_2$ to enhance the catalytic activity. To produce the Pd phase, both cells were then calcined in air at 723 K before measurement at 973 K with humidified H_2 fuel (3% H_2O).

Activity of Anodes with $Pd@CeO_2$ Catalyst. The electrochemical performance of a fuel cell with an LSCM/YSZ composite anode that was coated with a film of the $Pd@CeO_2$ nanostructures using the TEOOS grafting technique described above while operating on humidified H_2 at 973 K is shown in Figure 5. Data for an identical cell for which $Pd@CeO_2$ nanostructures were not added to the anode is also included in the figure. Note that the grafting technique resulted in a 0.01 wt % loading of $Pd@CeO_2$ particles based on the total weight and surface area of the anode (this corresponds to a 0.001 wt % loading of Pd). Prior to testing, the anode side of the cells was calcined in air at 723 K (which removes the capping alkyl groups required for the grafting procedure) and then reduced in humidified H_2 as the temperature was ramped up to 973 K.

As mentioned above, poor electrochemical performance was obtained when no catalyst was added, demonstrating that LSCM has minimal catalytic activity for H_2 oxidation. Good performance was obtained, however, for the cell in which $Pd@CeO_2$ had been added to the anode. This cell had a maximum power density of 0.30 W cm^{-2} and anode ASR of 0.52 Ω cm^2. It is noteworthy that the performance of this cell is similar to that of the cell in which the Pd was added by conventional means (Figure 4, Table 1), even though the total Pd loading was a 1000 times less. This demonstrates that only dopant levels of highly catalytically active metals, such as Pd, are required to enhance the catalytic activity of anodes which use metal oxide electronically conducting phases (e.g., LSCM) to acceptable levels.

Table 1. Electrochemical Performance of Cells with Various Anode Compositions[a]

cell no.	anode composition	TEOOS-treated?	calcination temp (K)	annealing conditions	anode ASR (Ω cm^2)	max power (W cm^{-2})
1	no catalyst	Y	723	O_2	3.46	0.10
2	no catalyst	N	723	O_2	2.95	0.12
3	$(NH_3)_4Pd(NO_3)_2$[b]	Y	723	O_2	0.24	0.39
4	$(NH_3)_4Pd(NO_3)_2$[b]	N	723	O_2	0.26	0.39
5	Pd	Y	723	O_2	0.50	0.30
6	Pd	Y	1123	O_2	1.30	0.19
7	Pd	Y	1073	H_2	0.83	0.23
8	Pd@CeO$_2$	Y	723	O_2	0.52	0.30
9	Pd@CeO$_2$	Y	1123	O_2	0.55	0.30
10	Pd@CeO$_2$	Y	1073	H_2	0.52	0.30

[a] The anodes were fabricated by impregnation. All the fuel cells are 45 wt % $La_{0.8}Sr_{0.2}Cr_{0.5}Mn_{0.05}O_3$–YSZ composite anodes. The anode ASR can be obtained by subtracting from the total resistance the ohmic (0.3 Ω cm^2) and cathode (0.2 Ω cm^2) contributions. [b] Different Pd precursor—$(NH_3)_4Pd(NO_3)_2$—and significantly more catalyst used (1 wt %).

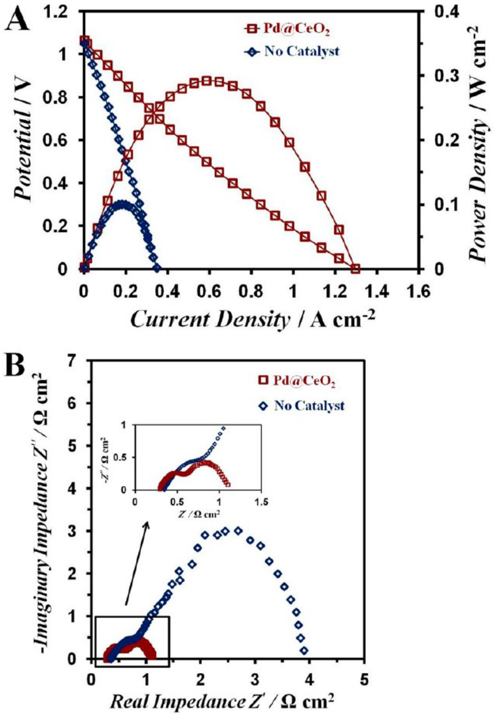

Figure 5. (A) *V*–*i* polarization curves and (B) electrochemical impedance spectra of cells with infiltrated 45 wt % LSCM–YSZ after treatment with TEOOS containing (red □) Pd@CeO$_2$ and (blue ◇) no catalyst. The cells were initially calcined at 723 K in air before measurement at 973 K with humidified H_2 fuel (3% H_2O).

Thermal Stability of Electrodes with Pd@CeO$_2$ Catalyst. Although high stability of LSCM/YSZ composite anodes with a grafted Pd@CeO$_2$ catalyst layer can be anticipated on the basis of the SEM results presented above, it was also evaluated in working fuel cells. In these tests, the anodes were calcined at temperatures above 1073 K, which is at least 100 K higher than the typical cell operating temperature (973 K) under both oxidizing and reducing conditions, to simulate performance degradation that would occur over a lengthy fuel cell test. For comparison purposes, cells with uncoated Pd nanoparticles added onto the TEOOS-treated LSCM–YSZ composite anode were also evaluated. Note that LSF–YSZ cathodes identical to those used here have previously been shown to be sufficiently stable that deactivation would not be expected to be significant over the relatively short duration tests reported below.[70]

As shown by the polarization curves and impedance data in Figure 6A,C, increasing the temperature at which the anode with the highly dispersed Pd@CeO$_2$ catalyst was calcined in air from 723 to 1123 K caused only small changes in performance, whereas operating with humidified H_2 fuel at 973 K with the maximum power density and anode ASR remaining close to 0.3 W cm^{-2}, and the anode ASR increased slightly from 0.52 to 0.55 Ω cm^2 (the performance for each cell including anode ASR values are summarized in Table 1). This is in sharp contrast to the cell with the uncoated Pd catalyst (Figure 6B,C) in which the maximum power density decreased from 0.3 to 0.19 W cm^{-2} and the anode ASR increased from 0.5 to 1.3 Ω cm^2 upon increasing the air calcination temperature from 723 to 1123 K. As shown by the polarization and impedance data in Figure 7, nearly identical results were obtained for a set of cells in which the anodes were aged by annealing in H_2 for 2 h at 1073 K. This treatment again had only a small effect on the performance of the anode with the Pd@CeO$_2$ catalyst, whereas a large decrease in performance was observed for the cell with the Pd nanoparticle catalyst.

Performance with CH_4 Fuel. Although the data presented above obtained with H_2 fuel provides considerable insight into the activity and stability of the Pd@CeO$_2$ nanostructures, one of the primary advantages of Pd@CeO$_2$/LSCM/YSZ electrodes over more conventional Ni–YSZ anodes is their ability to utilize hydrocarbon fuels. Thus, performance tests were also carried out using CH_4 as the fuel. Polarization curves for fuel cells with 0.01 wt % Pd@CeO$_2$ and with 0.01 wt % 2 nm uncoated Pd nanoparticles added to the anode are shown in Figure 8. The anodes were initially calcined at 723 K for 4 h in air and were then reduced in humidified H_2 as the temperature was ramped up to 973 K before the cells were operated in dry CH_4 at 973 K. For comparison purposes, a cell with an LSCM/YSZ anode with no added catalyst was also tested. As expected, this cell exhibited very poor performance, with a maximum power density of only 0.01 W cm^{-2}. Much higher performance was obtained from the cells with the added Pd@CeO$_2$ and Pd anode catalysts, which had maximum power densities of 0.11 and 0.15 W cm^{-2}, respectively. Note that this performance is lower than that obtained for H_2 fuel as a result of the higher activation barrier for methane oxidation. To investigate the thermal stability of the Pd and Pd@CeO$_2$ catalysts, the anodes were then calcined in air at 1123 K for 4 h, followed by measuring the cell performance at 973 K with CH_4 fuel. Consistent with the catalyst characterization studies presented above, this rapid thermal aging treatment caused the maximum power density of the cell with the uncoated Pd nanoparticle anode catalyst to decrease by 40%

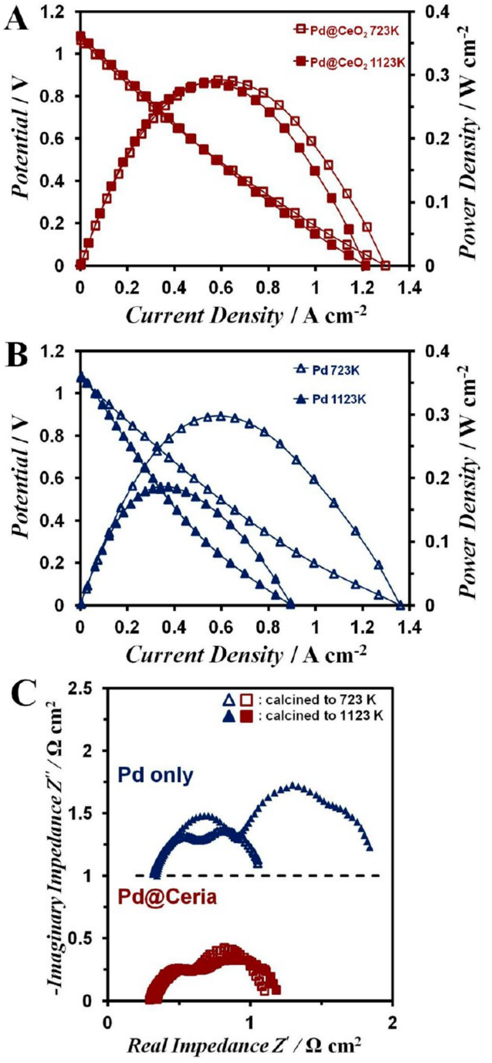

Figure 6. (A, B) V−i polarization curves and (C) electrochemical impedance spectra of cells annealed under oxidizing conditions at higher temperatures, with infiltrated 45 wt % LSCM−YSZ after treatment with TEOOS, containing infiltrated (panel A) Pd@CeO$_2$ nanoparticles annealed in air at (□) 723 and (■) 1123 K, (panel B) 2 nm uncoated Pd nanoparticles annealed in air at (Δ) 723 and (▲) 1123 K. The cells were operated at 973 K with humidified H_2 fuel (3% H_2O).

to 0.06 W cm^{-2}. In contrast, the maximum power density of the cell with the Pd@CeO$_2$ catalyst decreased by only 9% to 0.10 W cm^{-2}.

■ CONCLUSIONS

In this study, we have demonstrated the use of TEOOS as a surface modifier to aid in the dispersion of highly catalytic Pd@CeO$_2$ nanocomposites into porous SOFC anodes. SEM results show that a film of alkyl-capped Pd@CeO$_2$ particles can be deposited on TEOOS-treated anodes. In contrast to bare Pd particles, it was also demonstrated that high dispersion can be maintained after calcining in air at 973 K to oxidatively remove the organic groups and under the reducing conditions during fuel cell operation at similar temperatures. Furthermore, the high thermal stability of the dispersed Pd@CeO$_2$ particles was maintained after calcination in air at 1373 K, suggesting that long-term stability can be expected for SOFC operation using this precursor at 973 K.

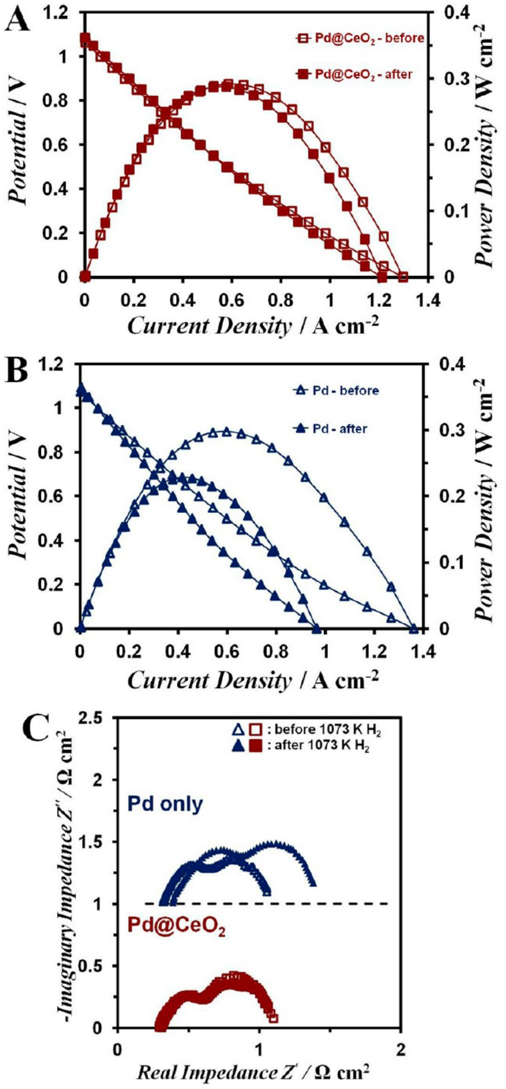

Figure 7. (A, B) V−i polarization curves and (C) electrochemical impedance spectra of cells annealed under reducing conditions at higher temperatures, with infiltrated 45 wt % LSCM−YSZ after treatment with TEOOS, containing infiltrated (panel A) Pd@CeO$_2$ nanoparticles (□) before and (■) after 1073 K treatment in humidified H_2, (Figure 7B) 2 nm uncoated Pd nanoparticles (□) before and (■) after 1073 K treatment in humidified H_2. The cells were initially calcined at 723 K in air before measurement at 973 K with humidified H_2 fuel (3% H_2O).

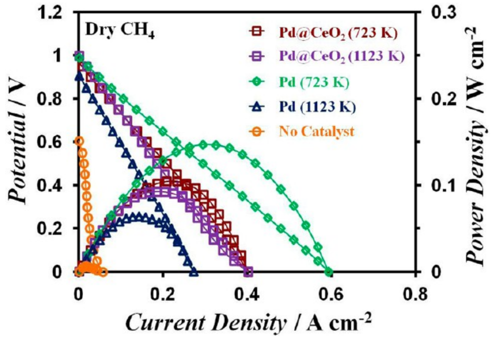

Figure 8. V−i polarization curves of infiltrated 45 wt % LSCM−YSZ after treatment with TEOOS, containing infiltrated (□) Pd@CeO$_2$ and (◇) 2 nm uncoated Pd nanoparticles calcined at 723 and 1123 K in air and (○) no catalyst. Measurements were taken at 973 K in dry CH_4.

An important aspect of the use of TEOOS as surface modifier to obtain a high dispersion of the Pd@CeO_2 particles is that it allows Pd weight loadings as low as 0.001% (based on the weight of the porous composite anode) to be used and still obtain high performance when operating on both H_2 and CH_4 fuels. In addition, high-temperature calcination under both oxidizing and reducing conditions in H_2 and CH_4 fuel caused only small changes in performance for the anode with the Pd@CeO_2 catalyst. This is in sharp contrast to the cell with the uncoated Pd catalyst, for which a large decrease in performance was observed when a similar high-temperature treatment was used.

AUTHOR INFORMATION

Corresponding Author

*E-mail: vohs@seas.upenn.edu.

Notes

The authors declare no competing financial interest.

ACKNOWLEDGMENTS

We acknowledge financial support from the U.S. Office of Naval Research, Grant No. N00014-11-1-0229.

REFERENCES

(1) Toebes, M. L.; Bitter, J. H.; van Dillen, A. J.; de Jong, K. P. *Catal. Today* **2002**, *76*, 33−42.

(2) Kim, H.; Lu, C.; Worrell, W. L.; Vohs, J. M.; Gorte, R. J. *J. Electrochem. Soc.* **2002**, *149*, A247−A250.

(3) Tao, S. W.; Irvine, J. T. S. *Chem. Rec.* **2004**, *4*, 83−95.

(4) Matsuzaki, Y.; Yasuda, I. *Solid State Ionics* **2000**, *132*, 261−269.

(5) Yokokawa, H.; Tu, H. Y.; Iwanschitz, B.; Mai, A. *J. Power Sources* **2008**, *182*, 400−412.

(6) Singhal, S. C. *Solid State Ionics* **2000**, *135*, 305−313.

(7) Steele, B. C. H.; Heinzel, A. *Nature* **2001**, *414*, 345−352.

(8) Iwanschitz, B.; Holzer, L.; Mai, A.; Schutze, M. *Solid State Ionics* **2012**, *211*, 69−73.

(9) Ettler, M.; Timmermann, H.; Malzbender, J.; Weber, A.; Menzler, N. H. *J. Power Sources* **2010**, *195*, 5452−5467.

(10) Vincent, A.; Luo, J. L.; Chuang, K. T.; Sanger, A. R. *J. Power Sources* **2010**, *195*, 769−774.

(11) Zhu, X. B.; Lu, Z.; Wei, B.; Liu, M. L.; Huang, X. Q.; Su, W. H. *Electrochim. Acta* **2010**, *55*, 3932−3938.

(12) Bierschenk, D. M.; Potter-Nelson, E.; Hoel, C.; Liao, Y. G.; Marks, L.; Poeppelmeier, K. R.; Barnett, S. A. *J. Power Sources* **2011**, *196*, 3089−3094.

(13) Liu, J.; Madsen, B. D.; Ji, Z. Q.; Barnett, S. A. *Electrochem. Solid St.* **2002**, *5*, A122−A124.

(14) Neagu, D.; Irvine, J. T. S. *Chem. Mater.* **2010**, *22*, 5042−5053.

(15) Antoni, L. *Mater. Sci. Forum* **2004**, *461−464*, 1073−1089.

(16) Arrive, C.; Delahaye, T.; Joubert, O.; Gauthier, G. *J. Power Sources* **2013**, *223*, 341−348.

(17) Atkinson, A.; Barnett, S.; Gorte, R. J.; Irvine, J. T. S.; McEvoy, A. J.; Mogensen, M.; Singhal, S. C.; Vohs, J. *Nat. Mater.* **2004**, *3*, 17−27.

(18) Dong, X. H.; Ma, S. G.; Huang, K.; Chen, F. L. *Int. J. Hydrogen Energy* **2012**, *37*, 10866−10873.

(19) Kim, G.; Corre, G.; Irvine, J. T. S.; Vohs, J. M.; Gorte, R. J. *Electrochem. Solid-State Lett.* **2008**, *11*, B16−B19.

(20) Kobsiriphat, W.; Madsen, B. D.; Wang, Y.; Marks, L. D.; Barnett, S. A. *Solid State Ionics* **2009**, *180*, 257−264.

(21) Adijanto, L.; Kungas, R.; Park, J.; Vohs, J. M.; Gorte, R. J. *Int. J. Hydrogen. Energy* **2011**, *36*, 15722−15730.

(22) Adijanto, L.; Padmanabhan, V. B.; Gorte, R. J.; Vohs, J. M. *J. Electrochem. Soc.* **2012**, *159*, F751−F756.

(23) Lee, S.; Kim, G.; Vohs, J. M.; Gorte, R. J. *J. Electrochem. Soc.* **2008**, *155*, B1179−B1183.

(24) Adijanto, L.; Padmanabhan, V. B.; Holmes, K. J.; Gorte, R. J.; Vohs, J. M. *J. Solid State Chem.* **2012**, *190*, 12−17.

(25) Adijanto, L.; Padmanabhan, V. B.; Kungas, R.; Gorte, R. J.; Vohs, J. M. *J. Mater. Chem.* **2012**, *22*, 11396−11402.

(26) Ge, X. M.; Chan, S. H.; Liu, Q. L.; Sun, Q. *Adv. Energy Mater.* **2012**, *2*, 1156−1181.

(27) Smith, B. H.; Gross, M. D. *Electrochem. Solid-State Lett.* **2011**, *14*, B1−B5.

(28) Marrero-Lopez, D.; Pena-Martinez, J.; Ruiz-Morales, J. C.; Perez-Coll, D.; Aranda, M. A. G.; Nunez, P. *Mater. Res. Bull.* **2008**, *43*, 2441−2450.

(29) Babaei, A.; Zhang, L.; Tan, S. L.; Jiang, S. P. *Solid State Ionics* **2010**, *181*, 1221−1228.

(30) Cowin, P. I.; Petit, C. T. G.; Lan, R.; Irvine, J. T. S.; Tao, S. W. *Adv. Energy Mater.* **2011**, *1*, 314−332.

(31) Kim, G.; Lee, S.; Shin, J. Y.; Corre, G.; Irvine, J. T. S.; Vohs, J. M.; Gorte, R. J. *Electrochem. Solid-State Lett.* **2009**, *12*, B48−B52.

(32) Gorte, R. J.; Park, S.; Vohs, J. M.; Wang, C. H. *Adv. Mater.* **2000**, *12*, 1465−1469.

(33) Kim, J. S.; Nair, V. V.; Vohs, J. M.; Gorte, R. J. *Scr. Mater.* **2011**, *65*, 90−95.

(34) Bierschenk, D. M.; Potter-Nelson, E.; Hoel, C.; Liao, Y. G.; Marks, L.; Poeppelmeier, K. R.; Barnett, S. A. *J. Power Sources* **2011**, *196*, 3089−3094.

(35) Bi, Z. H.; Zhu, J. H. *J. Electrochem. Soc.* **2011**, *158*, B605−B613.

(36) Gross, M. D.; Vohs, J. M.; Gorte, R. J. *J. Electrochem. Soc.* **2007**, *154*, B694−B699.

(37) Xiao, G. L.; Jin, C.; Liu, Q.; Heyden, A.; Chen, F. L. *J. Power Sources* **2012**, *201*, 43−48.

(38) Wang, Y.; Madsen, B. D.; Kobsiriphat, W.; Barnett, S. A.; Marks, L. D. *Microsc. Microanal.* **2007**, *13*, 100−101.

(39) Madsen, B. D.; Kobsiriphat, W.; Wang, Y.; Marks, L. D.; Barnett, S. A. *J. Power Sources* **2007**, *166*, 64−67.

(40) Fu, Q. X.; Tietz, F.; Sebold, D.; Tao, S. W.; Irvine, J. T. S. *J. Power Sources* **2007**, *171*, 663−669.

(41) Monteiro, N. K.; Noronha, F. B.; da Costa, L. O. O.; Linardi, M.; Fonseca, F. C. *Int. J. Hydrogen Energy* **2012**, *37*, 9816−9829.

(42) An, Y. T.; Choi, B. H.; Ji, M. J.; Lee, K. J.; Hwang, H. J. *Solid State Ionics* **2012**, *207*, 64−68.

(43) Kim, J. S.; Wieder, N. L.; Abraham, A. J.; Cargnello, M.; Fornasiero, P.; Gorte, R. J.; Vohs, J. M. *J. Electrochem. Soc.* **2011**, *158*, B596−B600.

(44) Farrauto, R. J.; Hobson, M. C.; Kennelly, T.; Waterman, E. M. *Appl. Catal., A* **1992**, *81*, 227−237.

(45) Wang, X.; Gorte, R. J.; Wagner, J. P. *J. Catal.* **2002**, *212*, 225−230.

(46) Ruettinger, W.; Liu, X. S.; Farrauto, R. J. *Appl. Catal., B* **2006**, *65*, 135−141.

(47) Spencer, M. S.; Twigg, M. V. *Annu. Rev. Mater. Res.* **2005**, *35*, 427−464.

(48) Lee, J. H.; Trimm, D. L. *Fuel Process. Technol.* **1995**, *42*, 339−359.

(49) Zhang, Z. L.; Tsipouriari, V. A.; Efstathiou, A. M.; Verykios, X. E. *J. Catal.* **1996**, *158*, 51−63.

(50) Nagai, Y.; Hirabayashi, T.; Dohmae, K.; Takagi, N.; Minami, T.; Shinjoh, H.; Matsumoto, S. *J. Catal.* **2006**, *242*, 103−109.

(51) Jacobs, G.; Patterson, P. M.; Zhang, Y. Q.; Das, T.; Li, J. L.; Davis, B. H. *Appl. Catal., A* **2002**, *233*, 215−226.

(52) Nishihata, Y.; Mizuki, J.; Akao, T.; Tanaka, H.; Uenishi, M.; Kimura, M.; Okamoto, T.; Hamada, N. *Nature* **2002**, *418*, 164−167.

(53) Twigg, M. V.; Spencer, M. S. *Appl. Catal., A* **2001**, *212*, 161−174.

(54) Euzen, P.; Le Gal, J. H.; Rebours, B.; Martin, G. *Catal. Today* **1999**, *47*, 19−27.

(55) Cargnello, M.; Jaen, J. J. D.; Garrido, J. C. H.; Bakhmutsky, K.; Montini, T.; Gamez, J. J. C.; Gorte, R. J.; Fornasiero, P. *Science* **2012**, *337*, 713−717.

(56) Yeung, C. M. Y.; Yu, K. M. K.; Fu, Q. J.; Thompsett, D.; Petch, M. I.; Tsang, S. C. *J. Am. Chem. Soc.* **2005**, *127*, 18010−18011.

(57) Wieder, N. L.; Cargnello, M.; Bakhmutsky, K.; Montini, T.; Fornasiero, P.; Gorte, R. J. *J. Phys. Chem. C* **2011**, *115*, 915−919.

(58) Yoon, K.; Yang, Y.; Lu, P.; Wan, D. H.; Peng, H. C.; Masias, K. S.; Fanson, P. T.; Campbell, C. T.; Xia, Y. N. *Angew. Chem., Int. Ed.* **2012**, *51*, 9543−9546.

(59) Cargnello, M.; Fornasiero, P.; Gorte, R. J. *Catal. Lett.* **2012**, *142*, 1043−1048.

(60) Adijanto, L.; Bennett, D. A.; Chen, C.; Yu, A. S.; Cargnello, M.; Fornasiero, P.; Gorte, R. J.; Vohs, J. M. *Nano Lett.* **2013**, *13*, 2252−2257.

(61) Hauch, A.; Jensen, S. H.; Bilde-Sorensen, J. B.; Mogensen, M. *J. Electrochem. Soc.* **2007**, *154*, A619−A626.

(62) Lankin, M.; Du, Y. H.; Finnerty, C. *J. Fuel Cell Sci. Technol.* **2011**, *8*, 054001.

(63) Zhang, T. S.; Ma, J.; Chen, Y. Z.; Luo, L. H.; Kong, L. B.; Chan, S. H. *Solid State Ionics* **2006**, *177*, 1227−1235.

(64) Park, S.; Gorte, R. J.; Vohs, J. M. *J. Electrochem. Soc.* **2001**, *148*, A443−A447.

(65) Adijanto, L.; Kungas, R.; Bidrawn, F.; Gorte, R. J.; Vohs, J. M. *J. Power Sources* **2011**, *196*, 5797−5802.

(66) Cargnello, M.; Montini, T.; Polizzi, S.; Wieder, N. L.; Gorte, R. J.; Graziani, M.; Fornasiero, P. *Dalton Trans.* **2010**, *39*, 2122−2127.

(67) Cargnello, M.; Wieder, N. L.; Montini, T.; Gorte, R. J.; Fornasiero, P. *J. Am. Chem. Soc.* **2010**, *132*, 1402−1409.

(68) Bakhmutsky, K.; Wieder, N. L.; Cargnello, M.; Galloway, B.; Fornasiero, P.; Gorte, R. J. *ChemSusChem* **2012**, *5*, 140−148.

(69) Corre, G.; Kim, G.; Cassidy, M.; Vohs, J. M.; Gorte, R. J.; Irvine, J. T. S. *Chem. Mater.* **2009**, *21*, 1077−1084.

(70) Wang, W. S.; Gross, M. D.; Vohs, J. M.; Gorte, R. J. *J. Electrochem. Soc.* **2007**, *154*, B439−B445.